Monte Carlo modeling of the response of NRC's ^{90}Sr/^{90}Y primary beta standard

T. Palani Selvam
Ottawa-Carleton Institute of Physics, Carleton University, Ottawa, K1S 5B6, Canada

P. R. B. Saull
Ionizing Radiation Standards, National Research Council of Canada, Ottawa, K1A OR6, Canada

D. W. O. Rogers[a)]
Ottawa-Carleton Institute of Physics, Carleton University, Ottawa, K1S 5B6, Canada

(Received 10 March 2005; revised 30 May 2005; accepted for publication 18 June 2005; published 21 September 2005)

The BEAMnrc/EGSnrc Monte Carlo code system is employed to develop a model of the National Research Council of Canada primary standard of absorbed dose to tissue in a beta radiation field, comprising an extrapolation chamber and ^{90}Sr/^{90}Y beta source. We benchmark the model against the measured response of the chamber in terms of absorbed dose to air, for three different experimental setups when irradiated by the ^{90}Sr/^{90}Y source. For the first setup, the chamber cavity depth is fixed at 0.2 cm and the source-to-chamber distance varied between 11 and 60 cm. In the other two cases, the source-to-chamber distance is fixed at 30 cm. In one case the response for different chamber depths is studied, while in the other case the chamber depth is fixed at 0.2 cm as different thicknesses of Mylar™ are added to the front surface of the extrapolation chamber. The agreement as a function of distance between the calculated and measured responses is within 0.37% for a variation in response of a factor of 29. In the case of dose versus chamber depth, the agreement is within 0.4% for the ISO-recommended nominal depths of 0.025–0.25 cm. Agreement between calculated and measured responses is very good (between 0.02% and 0.2%) for added Mylar foils of thicknesses up to 10.8 mg cm^{-2}. For larger Mylar thicknesses, deviations of 0.6%–1.2% are observed, which are possibly due to the systematic uncertainties associated with the restricted collisional stopping powers of air or Mylar used in the calculations. We conclude that our simulation model represents the extrapolation chamber and ^{90}Sr/^{90}Y source with adequate accuracy to calculate correction factors for accurate realization of dose rate to tissue at a depth of 7 mg cm^{-2} in an ICRU tissue phantom, despite the fact that the uncertainties in the physical characteristics of the source leave some uncertainty in certain calculated quantities. © *2005 American Association of Physicists in Medicine*. [DOI: 10.1118/1.1997347]

I. INTRODUCTION

The extrapolation chamber is one of the preferred experimental devices for measuring dose rate in a tissue-equivalent phantom resulting from high energy radiotherapy beams (to estimate the entrance skin dose) and weakly penetrating radiations such as beta radiation and low energy x rays. Extrapolation chambers are usually made of a roughly tissue-equivalent material such as polymethylmethacrylate (PMMA), containing an air-filled cavity. The axial dimension of this air cavity is referred to as chamber depth, and can be varied by adjusting the distance between the two collecting electrodes. In practice, current measurements are carried out at a series of depths. These current values as a function of depth are fitted to determine the slope at the limit of zero depth. The absorbed dose rate at the surface of the phantom is then determined using the Bragg-Gray or Spencer-Attix relationships and an appropriate set of correction factors. A complete description of the application of cavity theory to the use of the extrapolation chamber in beta radiation dosimetry is reported in the literature.[1–5]

Protection-level beta dosimetry involves the measurement of low dose rates at distances of 10–50 cm from a beta radiation source.[4] The quantity of interest is the dose rate to tissue at a depth of 7 mg cm^{-2}, D_t(7 mg cm^{-2}), in an ICRU (International Commission for Radiation Units and Measurements) tissue-equivalent phantom. The Physikalisch-Technische Bundesanstalt (PTB) established a primary standard based on an extrapolation chamber for this purpose.[2]

In the early 1980s, the National Research Council of Canada (NRC) developed an extrapolation chamber[3] based on the design by the PTB.[2] In 1984, NRC purchased a beta radiation secondary standard for absorbed dose from Buchler GmbH, Braunschweig, FRG, identified as No. 45. The standard includes a ^{90}Sr/^{90}Y source whose nominal activity in May 1984 was 1.85 GBq. The NRC national standard established in 1986[3] was found to be in good agreement with the measurements by the PTB using the same sources.[3]

For the present study, measurements using the NRC extrapolation chamber were carried out in a ^{90}Sr/^{90}Y beta field for three different situations. The goal of the present work is to develop a Monte Carlo-based model of the NRC ^{90}Sr/^{90}Y beta source and extrapolation chamber, and in the future to calculate the various correction factors needed for accurate

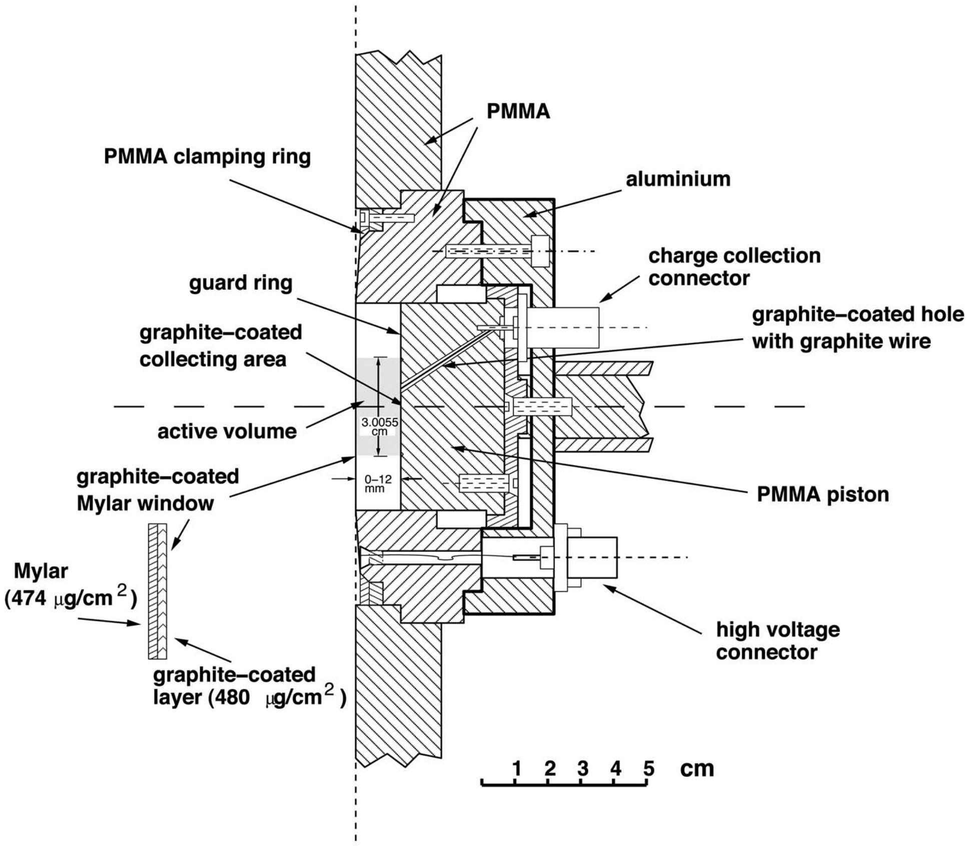

FIG. 1. A schematic diagram of the NRC extrapolation chamber. The only dimension that changes when the PMMA piston is moved is the chamber depth. Drawing is not exactly to scale.

estimation of $D_t(7\ \mathrm{mg\ cm}^{-2})$ in the ICRU phantom. As a first step, it is essential that the model is benchmarked against the measured responses.

II. NRC EXTRAPOLATION CHAMBER AND RADIOACTIVE SOURCE

The NRC extrapolation chamber[3] has cylindrical geometry and is made predominantly of PMMA (see Fig. 1). It is mounted such that its thin, graphite-coated-Mylar™ entrance window is fixed in line and flush with the front face of a $46\ \mathrm{cm} \times 46\ \mathrm{cm} \times 2.4\ \mathrm{cm}$ PMMA phantom. The radius of the entrance window is 3.035 cm, and the areal thicknesses of Mylar and graphite are 474 and 480 $\mu\mathrm{g\ cm}^{-2}$, respectively, for a total areal thickness of $(954\pm95)\ \mu\mathrm{g\ cm}^{-2}$. The graphite layer serves as one electrode, while the collecting electrode (maintained at ground potential) is a movable cylindrical piston, made of PMMA, coated by a layer of graphite whose areal density and radius are 480 $\mu\mathrm{g\ cm}^{-2}$ and 3.035 cm, respectively. Inscribed in the electrode is a circular groove at radius 1.5027 cm which defines the guard ring and the sensitive ion-collection area to be $(7.094\pm0.001)\ \mathrm{cm}^2$. This area and the separation between the electrodes, known as the nominal chamber depth, l, together define the sensitive ion-collection air volume. In the measurements, when the micrometer displays zero depth, an actual depth of $15\pm2\ \mu\mathrm{m}$ is realized. Therefore, the true chamber depth is $l'=l+(15\pm2)\ \mu\mathrm{m}$ and the sensitive ionization volume is $V=\pi r^2 l'$. The influence of the uncertainty in this depth offset on the experimental response can be significant for small depths.

A diagram of the $^{90}\mathrm{Sr}/^{90}\mathrm{Y}$ beta source modeled in our Monte Carlo study is shown in Fig. 2. The source is a cylinder of stainless steel, with a radius of 0.495 cm and an overall thickness of 0.24 cm. Within this, centered on the symmetry axis, is another cylindrical region of silver (Ag) with a radius of 0.355 cm and thickness of 0.05 cm, lying at a nominal depth of 0.01 cm from the surface of the stainless-steel cylinder. $^{90}\mathrm{Sr}/^{90}\mathrm{Y}$ is distributed in carbonate form throughout a 20-μm-thick slice of this Ag region, 48 μm below the surface of the Ag.

The calibration jig to hold the sources is based on a design by Owen[6] and is shown in Fig. 3. The calibration jig includes an electrically controlled aluminium (Al) shutter (thickness 0.7 cm) and four cylindrical stainless-steel rods (each has a length of 10.5 cm and a diameter of 3 mm) extending toward the chamber, for holding an optional beam-flattening filter (not used for the present measurements). The rods are fixed to the source stand and are positioned symmetrically about, and parallel to, the source symmetry axis, at a radial distance of 14.5 cm from it.

III. MEASUREMENTS WITH THE EXTRAPOLATION CHAMBER

Charge measurements with the NRC extrapolation chamber were made with a Keithley model 642 electrometer as a

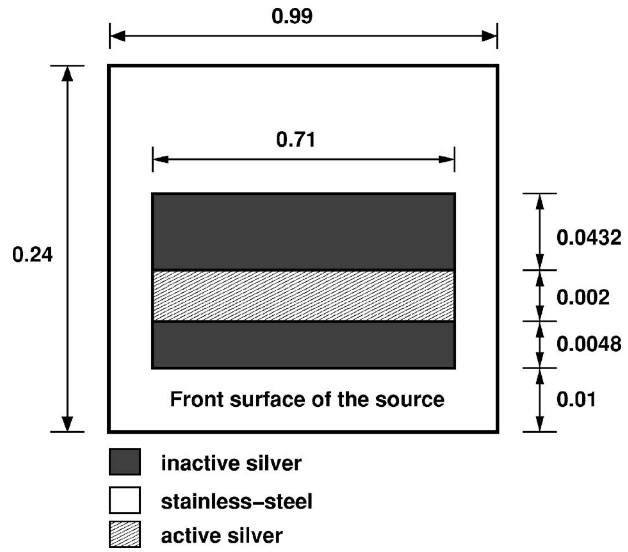

FIG. 2. A cross-sectional sketch of the $^{90}Sr/^{90}Y$ beta source as simulated in our Monte Carlo calculations. The dimensions shown are in centimeters and are not to scale. In particular, the silver is a thin foil near the front surface of the stainless steel. Transport of electrons in the source regions behind the first 0.025 cm of the rear inactive silver layer was ignored in the Monte Carlo calculations as particles from this region could not reach the front face.

function of time with sub-millisecond accuracy, and the data fitted to determine currents for further analysis. Measurements were carried out after at least 24 h of settling time to allow the system to stabilize. Leakage currents under stable conditions were found to be at most 0.2 fA. For all exposures (shutter open), leakage currents were redetermined during a 10 s period both prior and subsequent to irradiation, and never found to be more than 0.1% of the current measured during irradiation. Shutter-open times varied from 6 to 20 s, depending upon the configuration. For all measurements an electric field of 100 V/cm was applied to the chamber, and data were collected with both polarities in order to correct for the presence of a parasitic current due to beta rays absorbed directly in the chamber electrodes. The procedure was repeated at least five times for each distinct configuration, and the resulting set of values used to determine a raw current value with estimated statistical uncertainty to assign to the associated data point. The final current, I, for the point was then obtained by applying corrections to the raw current for ion-collection loss, source decay (using a half life of 28.79 years, with all data referenced to Oct 2 2002) and environmental conditions (referenced to $T=22\ ^\circ\mathrm{C}$ and $P=101.325$ kPa). This current was converted to absorbed dose to air (expressed in units of Gy/s), D_a, using

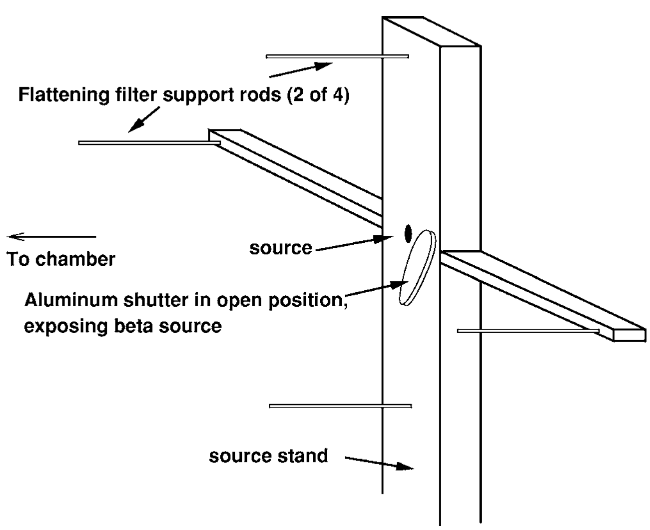

FIG. 3. A schematic diagram of the calibration jig of NRC's $^{90}Sr/^{90}Y$ primary beta standard. The aluminum shutter is 0.7 cm thick and is 0.01 cm away (axially) from the front face of the source when it is in open position. The supporting rods are made of stainless steel and are provided for holding an optional beam-flattening filter (not used for the present measurements). The length and diameter of each of the rods are 10.5 and 0.3 cm, respectively. These rods are positioned symmetrically about, and parallel to, the source symmetry axis, at a radial distance of 14.5 cm.

$$D_a = \frac{I \times (W/e)_{\mathrm{air}} \times k_h}{V \times \rho_{\mathrm{air}}}, \tag{1}$$

where $(\mathrm{W/e})_{\mathrm{air}}$ is 33.97 J/C, V is the active volume of the chamber in cm^{-3}, $k_h=0.997$ is the factor for correcting the reading in humid air to that for dry air,[3] and ρ_{air} is the density of dry air under reference conditions $(1.196\times10^{-6}\ \mathrm{kg/cm^3})$.

Using this procedure, several dose rate measurements were made for each of the following three experimental setups.

Experiment 1: Dose rate to air in a cavity of fixed depth $l'=0.2015$ cm for different source-to-chamber distances, y, where y is the distance between the front face of the source and the front surface of the entrance window of the extrapolation chamber. The values of y ranged from 11 to 60 cm.

Experiment 2: Dose rate to air in a cavity at fixed distance, $y=30$ cm, for cavity depths, l', ranging from 0.0215 to 0.4015 cm.

Experiment 3: Dose rate to air in a cavity of depth $l'=0.2015$ cm and distance $y=30$ cm, for different thicknesses of Mylar foils applied to the front face of the chamber.

The values for the current I ranged from 235 fA (experiment 2 at smallest depth) to 15.4 pA (experiment 1 at closest distance). The magnitude of the parasitic current ranged from 4% to 6% of the current I for experiments 1 and 3, whereas for experiment 2 it ranged from 3% (at largest depth) to 54% (at smallest depth). These numbers are typical of extrapolation chamber measurements.

The measurements were carried out so that there was a common point ($y=30$ cm, $l'=0.2015$ cm, and no added Mylar foil). The three different dose rates obtained for this common configuration were consistent within their statistical uncertainties, despite the fact that the data were collected over a period spanning nearly two years.

For experiment 3, Mylar foils of radius 10 cm with varying thickness were mounted with nylon screws directly on the face of the phantom, thus completely covering the entrance window. To ensure uniform contact, a PMMA ring (thickness 0.15 cm, inner and outer diameters of 17 and 20 cm, respectively) was screwed down on top of the Mylar absorbers.

Statistical uncertainties for the measurements are quoted for one standard deviation $(k=1)$ and incorporate the fluctuations in the current measurements observed for each data point. These were normally 0.1% for experiments 1 and 2, and never more than 0.2%. Owing to charge effects associated with the addition of Mylar foils to the front face of the chamber, the statistical uncertainty associated with experiment 3 is higher, at 0.2%. Systematic uncertainties (also $k=1$), are dominated by: an uncertainty of 0.2 mm on the positioning of the chamber at each value of y, as well as a global (correlated) uncertainty on the distance scale of 0.2 mm; and a global uncertainty in the depth offset value of 2 μm which affects each depth measurement in a correlated manner and propagates to a correlated uncertainty in the measured dose rate values. The positional uncertainty leads to an uncertainty in the measured dose rate value of 0.36% at $y=11$ cm, but only 0.06% at $y=60$ cm. The depth offset uncertainty leads to an uncertainty in the measured dose rate value of 0.93% for the smallest depth of 0.0215 cm, but only 0.05% for the largest depth of 0.4015 cm. The application of these systematic uncertainties in the analysis of the data is discussed in Sec. V C.

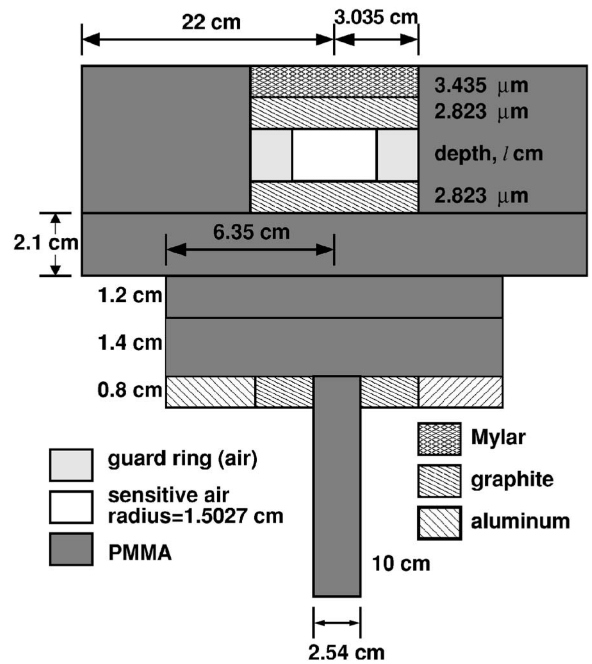

FIG. 4. A schematic diagram of the Monte Carlo model of the NRC extrapolation chamber.

IV. DESCRIPTION OF MONTE CARLO MODEL

The EGSnrc-based[7] BEAMnrc[8,9] is a well-established Monte Carlo code system which has been extensively used in modeling radiotherapy beams.[10–13] We have employed this code system to model the three experimental setups described in Sec. III. Modeling of experiments 1, 2, and 3 is referred to as simulations 1, 2, and 3, respectively. For simulation 2, l' was varied from 0.0215 to 1.0015 cm. For simulation 3, the thicknesses of Mylar foils used in the Monte Carlo calculations are in accordance with experimental considerations. Mylar foils were assumed to be in contact geometry with the entrance window of the extrapolation chamber. The PMMA ring used to secure the Mylar foils as present in the experiment was also modeled in the Monte Carlo simulations.

For the Monte Carlo simulations we utilized the following component modules (CMs) of the BEAMnrc code system: CONESTAK to model the source, two BLOCK modules to model the Al shutter (0.01 cm away from the front face of the source) and the four stainless-steel support rods, FLATFILT to model the components of the NRC extrapolation chamber including Mylar foils for simulation 3, and SLABS to model the air between ends of the support rods and extrapolation chamber. These CMs are cylindrically symmetric and had a common axis. The intervening medium between the CMs is air which extends to 100 cm off axis.

The Monte Carlo model of the extrapolation chamber shown in Fig. 4 is not significantly different from the real chamber. In the real chamber, when the PMMA piston is moved for changing the depth, the only dimension that changes is the chamber depth. However, in the case of Monte Carlo model, the overall thickness of PMMA changes with the chamber depth. This simplification of the geometry is not important as the thickness of PMMA involved is effectively infinite for ^{90}S/^{90}Y beta-rays.

The modeling of the support rods was done in such a way that the cross section of each rod was nearly circular and its mass the same as that of a real rod. The dose contribution from the rods varied between 0.05% and 0.07% depending upon y. The dose contribution from the shutter in an open position was about 1%, independent of y. However, an investigation for the case $y=30$ cm and $l'=0.2015$ cm, declaring the Al shutter region to be air, revealed that the electrons traversing through this air region contributed about 0.4% to the total dose. Thus the presence of the Al shutter in open position effectively makes a contribution of only 0.6%, in this case.

All Monte Carlo simulations utilized the PRESTA-II electron-step-length algorithm and EXACT boundary crossing algorithm.[7] Before initiating the main simulations we carried out some exploratory simulations.

We carried out simulations of energy transmitted through the front face of the source involving only the source, for the purpose of selecting appropriate values of the region-specific electron-transport-cut-off parameter, ECUT. By this approach the detailed transport of electrons in select source regions can be avoided without losing accuracy for the particles leaving the source. We found that only transport in a 0.025-cm-thick layer of inactive Ag behind the active Ag layer affected particles leaving the front face. This enabled us to ignore transport in the regions behind this 0.025-cm thick inactive Ag layer by setting ECUT=3 MeV, resulting in a gain in efficiency of about 5%.

Electron range rejection[8] was employed for all calculations. To verify that using electron range rejection did not affect the contaminant photon dose from bremsstrahlung production, we did a calculation without electron range rejection. In this mode, the contribution from photons to the total cavity dose was found to be only 0.02%. The calculation repeated with range rejection did not alter the total cavity dose when compared to not using range rejection. However, the efficiency was improved by a factor of 3 when using range rejection.

Based on auxiliary calculations carried out for the case $y=30$ cm and $l'=0.2015$ cm (the source was surrounded with Al cylinders of different radii), we have estimated that the maximum contribution to the dose from the support stand is of the order of 0.1% of the total dose. Since this is so small and we cannot accurately include this aspect of the geometry in the simulation, we have not modeled it.

While simulating the extrapolation chamber we generally set the low energy threshold for electron transport to ECUT=521 keV (10 keV kinetic energy) and the photon-transport-cut-off parameter to PCUT=1 keV. For the air-cavity and those regions in close proximity to it such as the entrance window (Mylar and graphite layers) and the collecting electrode (graphite layer), ECUT was set to 512 keV (1 keV kinetic energy). The range of 10 keV electrons in low Z materials is about 2.9×10^{-4} g cm^{-2} (0.24 cm in air) which is less than the thickness of the graphite, Mylar, and air regions around the cavity. Hence, the overall calculation of the dose in the air cavity is equivalent to tracking electrons to 1 keV everywhere.

In the case of simulation 1, the extrapolation chamber is irradiated at various distances. In order to reduce the computation time, we adopted a variance reduction technique, namely, particle splitting.[8] Each electron was split into n electrons whenever it crossed a plane 0.5 cm upstream of the entrance window of the extrapolation chamber (for the $y=11$ cm case, the splitting plane was at 0.1 cm in front of the entrance window, as the support rods themselves extend up to 10.5 cm), where n was varied between 5 and 100. We obtained a maximum gain in efficiency of approximately 2.5 when $n=10$, independent of y. Auxillary calculations revealed that the dose estimates were insensitive to whether particle splitting was used or not and also insensitive to the plane at which the particles were split.

Simulations 2 and 3 involve fixed y, so the calculation of dose in the air cavity could be carried out in two steps. First, the particles were transported through the source, Al shutter, stainless-steel rods and intervening air medium out to a predefined scoring plane located 1 cm before the extrapolation chamber. The particle phase space parameters, i.e., position, energy, direction, weight, particle type, and LATCH values to track the particle's history,[8,9] were scored out to a 40 cm radius in the scoring plane. For this purpose we had set up a separate model of the extrapolation chamber. As BEAMnrc scores phase space parameters at the back of a module, the SLABS module was positioned in such a way that its back was at 29 cm from the front face of the source and no material was present behind it. The chosen values of ECUT and PCUT were 521 and 1 keV, respectively. The phase-space data were collected at 1 cm upstream of the distance of interest (30 cm) so that future calculations may be carried out with no entrance window on the extrapolation chamber, yet maintaining an effective cutoff of 1 keV at the surface of the chamber by using ECUT=1 keV in the last 1 cm of air. Also, for front wall calculations, we need to be able to add material (Mylar foils) to the front of the detector, thus decreasing the 1 cm gap. The phase space parameters were stored in 10 separate phase-space files, each of size 800 Mbytes and containing 29 million particles.

The selection of a radius of 40 cm at the scoring plane was based on two separate Monte Carlo calculations with a cavity depth of 0.2015 cm. The first calculation created 10 phase-space files with a radial extension of 100 cm at 29 cm. These phase-space files were utilized in the second Monte Carlo calculation for dose calculation in the air cavity with the extrapolation chamber positioned 1 cm from the phase-space plane. To study a worst case situation where the chamber had no front and side walls, we declared these walls to be air in the simulation. In order to calculate the contribution from particles at different radii in the phase-space file to the total cavity dose, we defined an air layer, 1 μm in thickness, at 29.1 cm. This thin air layer extended out to a 100 cm radius and was was divided into five radial regions (width of 20 cm each). The individual radial regions were assigned different LATCH bits to determine the dose contribution from these geometrical regions to the total cavity dose. We found that the electrons in the radial bin 20–40 cm contributed 0.03% of the total cavity dose, and the radial bins beyond 40 cm made practically zero contribution. We thus only stored phase-space data out to 40 cm radius for the main runs.

In a second stage, the particles contained in the phase-space files were transported through the extrapolation chamber for simulations 2 and 3. We included the 29-cm-thick air column behind the phase-space plane when using the phase space as a source. To confirm the accuracy of using phase-space files for calculating air-cavity dose in simulations 2 and 3, we calculated the dose in the air cavity of depth $l'=0.2015$ cm, using these files. The dose value agreed within the statistics of ±0.22% with the corresponding value obtained in simulation 1. Exclusion of the 29-cm-thick air column would result in underestimation of the cavity dose by 1%. We conclude that the phase-space files can safely be used for simulations 2 and 3. Depending upon the type of simulation and uncertainty desired, the computation time varied between 10 and 1200 h on 2.4 GHz Pentium Xenon CPUs.

The uncertainty in the thickness of stainless-steel material on the front of the source is as large as 5%. However, to show any possible influence on results, we repeated some of our Monte Carlo simulations (discussed in the following) with 25% more stainless steel on the front, i.e., 0.0125 cm instead of 0.01 cm.

The energy spectrum of the ^{90}Sr/^{90}Y beta source used for the Monte Carlo calculations was taken from ICRU report

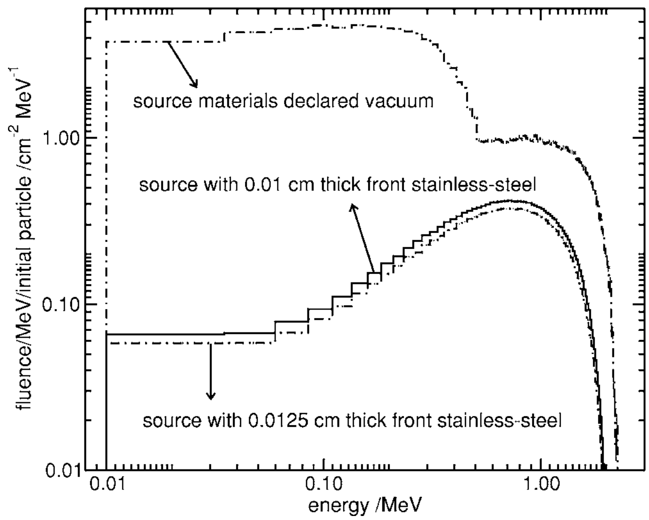

FIG. 5. Energy fluence spectra of electrons transmitted through the front face of the ^{90}Sr/^{90}Y beta source in a circular region of radius 0.355 cm centered about the source axis. A 25% increase in the thickness of the stainless-steel cover causes a 10% decrease in the fluence but has little effect on the spectral shape. Also shown is the spectrum obtained when the source materials are declared vacuum.

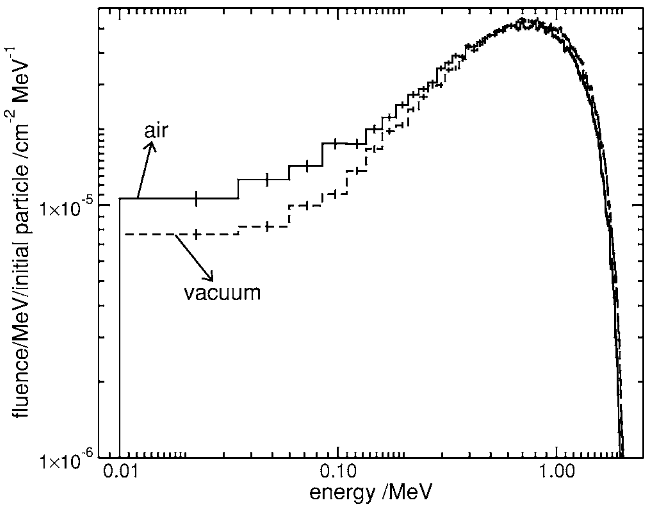

FIG. 6. Energy fluence spectra of electrons scored at a phase-space plane positioned 29 cm from the ^{90}Sr/^{90}Y source when the intervening medium between the source and the scoring plane was air or vacuum. The spectra are averaged over a circular region of radius 3.035 cm centered about the source axis.

56.[14] In the Monte Carlo calculations, the active source region was assumed to be 100% Ag, as the presence of radioactive materials (strontium and yttrium) amounts to less than a 1 μm (it depends on the activity of the source). The densities assumed in the calculations for graphite, Mylar, stainless-steel, Ag, and air are 1.7, 1.38, 8.06, 10.5, and 1.205×10^{-3} g/cm^3, respectively.

V. RESULTS AND DISCUSSION

A. Energy absorption in and escape from the source

The total available energy per initial particle calculated based on the average energy of the initial spectrum (563 keV) is 9.01×10^{-14} J/initial particle. Of this energy, 79% is absorbed by the source materials themselves, viz., 67% by the Ag layers (the active layer alone accounts for 15%), 0.9% by the 0.18-cm-thick rear stainless-steel layer, and 9% by the 0.01-cm-thick front stainless-steel layer. The fraction of energy escaping in the backward and radial directions is 0.42% and 0.35%, respectively. The energy fraction escaping in the forward direction is 20%, of which only 0.3% is due to the ^{90}Sr component of the ^{90}Sr/^{90}Y beta spectrum. When the front stainless-steel thickness was increased to 0.0125 cm, the energy escaping through the front face decreased to 17.7%, i.e., less by 12% relative to that for a thickness of 0.01 cm.

B. Energy distribution of electrons and mean energy

Figure 5 presents the differential fluence spectra of electrons as they leave the front face of the source and in the same geometry with only vacuum. The spectra are averaged over a circular region of radius 0.355 cm centered about the source axis. Note the marked change in the shape between vacuum and full-simulation cases: 62% of the electrons fall below 500 keV in the initial spectrum (vacuum case), compared to 23% for the full-simulation. The spectrum is also shown for the case where the stainless-steel cover is made an extra 25% thicker than the nominal thickness of 0.01 cm. The figure makes clear that the spectral shape depends little on the details of the material thickness covering the activity, although the absolute fluence is quite sensitive to this quantity (the total number of particles transmitted in the case of a 0.0125-cm-thick stainless-steel front was 10% less).

Figure 6 presents the differential fluence spectra of electrons at the plane positioned 29 cm from the source, averaged over a circular region of radius 3.035 cm centered about the source axis. Also shown in this figure is the spectrum corresponding to the actual source in vacuum, provided to show the influence of the air.

We also calculated the fluence-weighted mean energies (hereafter mean energy refers to fluence-weighted) using the phase-space data collected at the surface of the source with the EGSnrc-based user-code FLURZnrc.[15] The values calculated at the front surface of the source averaged over the circular region of radius 0.355 cm centered about the source axis for the stainless-steel front thicknesses of 0.01 and 0.0125 cm are 855 and 845 keV, respectively. Similarly, the on-axis mean energies calculated for the stainless-steel front thickness of 0.01 cm, as a function of distance from the source in a cylindrical air phantom of dimensions 100 cm $\times$ 100 cm, decrease as y increases from 11 to 60 cm. For example, the mean energies in air (averaged over a circular region of radius 3.035 cm and a thickness of 0.2015 cm) at y=11, 30, and 60 cm are 857±0.1% keV, 827±0.1% keV, and 783±0.2% keV, respectively, whereas in vacuum the value is 888±0.1% keV, independent of y (within statistics of ±0.1%).

TABLE I. Values of α [extracted from Eq. (2)] and χ^2/df, for the investigated cases. These values are based on the calculated and measured responses. The response refers to Monte Carlo calculated dose (Gy/initial particle) or measured dose rate (Gy s^{-1}) to the air in the extrapolation chamber cavity. Global fits (cases 4 and 4a) include all the uncertainties associated with the measurements. Cases 1, 3, and 3a do not include a systematic uncertainty of 0.1% in the depth offset at the chamber depth of 0.2015 cm. Cases 2, 2a, 3, and 3a do not include 0.13% positional uncertainty present at source-to-chamber distance of 30 cm. The variable n is the number of data points in each comparison.

Case	n	$\alpha \times 10^9$ electrons/s	α value normalized to overall fit (case 4a)	χ^2/df
Local fits				
1. Response vs distance	10	2.4741±0.09%	0.9999	0.55
Response vs depth				
2. All depths	15	2.4780±0.12%	1.0015	2.39
2a. Depths 0.03–0.25 cm	12	2.4721±0.09%	0.9991	0.72
Response vs Mylar thickness				
3. All thicknesses	20	2.4685±0.11%	0.9976	4.70
3a. Thickness up to 10.8 mg cm^{-2}	10	2.4774±0.07%	1.0012	0.30
Global fits				
4. All response points	43	2.4719±0.07%	0.9990	1.18
4a. Less 3 depths and 10 Mylar thicknesses	30	2.4744±0.08%	⋯	0.30

C. Experiment vs Monte Carlo calculations

We adopt a unified approach to normalizing the Monte Carlo and experimental data to each other. The Monte Carlo simulations yielded 43 dose values denoted by $D_{MC}(i)$, $1 \leqslant i \leqslant 43$, expressed in units of Gy/initial electron. The corresponding measured dose rate values are denoted by $D_M(i)$, expressed in units of Gy/s. Hence, a ratio between the i^{th} value of measurement and calculation, defined by $\alpha(i)=D_M(i)/D_{MC}(i)$, yields the number of electrons emitted by the source per second, or equivalently, represents the activity of the source. Perfect agreement between all the measurements and Monte Carlo values would predict a constant value of $\alpha(i)$. The Monte Carlo simulations 1–3 (and the corresponding measurements) have a common point, i.e., $y=30$ cm and $l'=0.2015$ cm. One could select a value of α from the series of $\alpha(i)$, preferably the one derived from the common point. This is denoted by α_0. We obtained, $\alpha_0=2.4748\times 10^9 \pm 0.12\%$ electrons/s. When each of the values of $D_{MC}(i)$ is scaled by α_0, the resultant quantity $[\alpha_0 \times D_{MC}(i)]$ represents dose rate, expressed in units of Gy/s. Therefore, a direct comparison between measurement and calculation is possible. We have adopted an alternative, yet equivalent approach. Instead of assigning special importance to a particular point (e.g., $y=30$ cm and $l'=0.2015$ cm), we derive α using a least-square fit and minimizing

$$\chi^2 = \sum_{i=1}^{n} \frac{(D_M(i) - \alpha D_{MC}(i))^2}{s_i^2}, \tag{2}$$

where n is the number of data points compared, $s_i^2=s_{MC(i)}^2+s_{M(i)}^2$, $s_{MC(i)}$ and $s_{M(i)}$ are the absolute uncertainties associated with i-th calculated or measured response, respectively, where both $s_{MC(i)}$ and $s_{M(i)}$ are expressed in units of Gy s^{-1}. The $s_{M(i)}$ values include both measurement uncertainty as well as the systematic uncertainties present in the measurements (see Sec. III).

Table I reports the values of α and the corresponding values of χ^2/df derived from Eq. (2) for different cases, each of which includes the response at the common point. The local fits such as cases 1, 3, and 3a do not include a ±0.1% uncertainty in the depth offset at the depth of 0.2015 cm, because the chamber depth was not varied for these measurements. Similarly, the positional uncertainty of 0.13% present at $y=30$ cm was not included in the local fits for cases 2, 2a, 3, and 3b since the chamber was not moved for these measurements. Exclusion of the above-mentioned uncertainties for the local fits was necessary as these uncertainties are correlated and introduce a common shift of all measured data points. Also, if the responses of these cases are normalized against each other the effect of these uncertainties cancel out. However, for the global fits (cases 4a and 4b), all the uncertainties are important to estimate α accurately, and therefore they are included. The values shown in the fourth column of Table I are the α values normalized to the α value obtained from the global fit (case 4a). Exclusion of five dose versus depth points in cases 2a and 4a is motivated by the fact that ISO (International Standards Organization) recommends using only the range of nominal chamber depths from 0.025 to 0.25 cm for measurements.[4] We also excluded 10 dose points of dose versus Mylar corresponding to the thickest Mylar regions in the cases 3a and 4a, in order to avoid any possible systematic uncertainties associated with the stopping powers used in the calculations (discussed in the following) affecting the α value. Cases 2 and 3 did not satisfy the χ^2 test at the 95% confidence level as the χ^2 values of these cases were larger than the corresponding critical values of χ^2 at the 0.05 significance level. All the other cases passed the same χ^2 test. The differences between the values of α for the investigated cases are consistent with the uncertainties associated with them. We use the value of $\alpha=2.4744\times 10^9 \pm 0.08\%$ extracted from the global approach (case 4a) for scaling $D_{MC}(i)$ as this parameter represents the three different experimental situations. This value of α corresponds to an activity of 1.237 GBq (since there are two beta particles per disintegration), which is consistent with the estimated value of 1.2±0.1) GBq as of Oct 2 2002.

We introduce a global normalization by selecting the scaled Monte Carlo calculated dose rate value corresponding to the common point. This scaled calculated value is denoted by D_{MC} and is consistent with the corresponding measured value well within the statistics. The advantage of normalizing based on the calculated data is that they are free from systematic uncertainties related to distance or offset which are present in the measurements.

1. Response vs source-to-chamber distance

Figure 7 presents a comparison of scaled Monte Carlo calculated and measured absolute dose rate values at various y in an air cavity of depth $l'=0.2015$ cm. The absolute dose value decreases by a factor of 29 when y is increased from 11 to 60 cm. Figure 8 presents the same data multiplied by y'^2 (where $y'=y+0.10075$ cm, the distance between source and the centre of the air cavity) and normalizing the same to the value $D_{\mathrm{MC}}\times(30.10075)^2$. The agreement varies between ±0.02% and ±0.37% (most values within ±0.1%). Also shown is the on-axis dose to air obtained when the encapsulated source irradiated a 100 cm × 100 cm cylindrical air phantom (normalized at 30.100 75 cm). If we compare the absolute values of the dose to air in the same volumes with or without the extrapolation chamber present, we find the extrapolation chamber materials enhance the dose to air by about 14% when $y=11-40$ cm and 13% at $y=50$ and 60 cm. However, the figure demonstrates that the variation of dose with distance is remarkably similar in both cases.

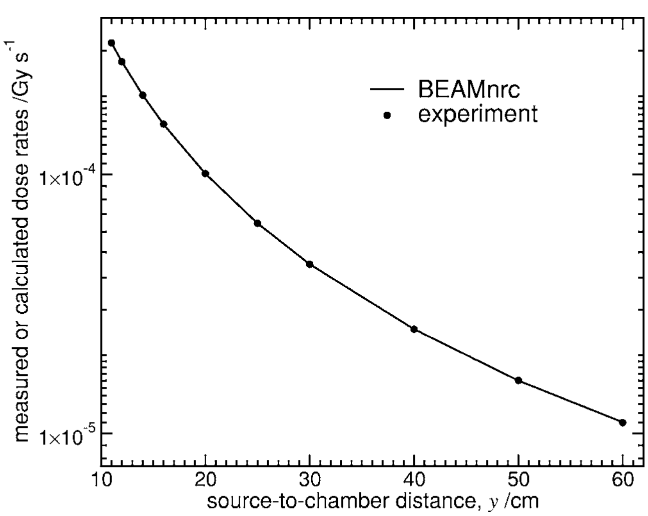

FIG. 7. Comparison of scaled Monte Carlo calculated and measured absolute dose rates as a function of source-to-chamber distance, y. The value used for scaling calculated values is $\alpha=2.4744\times10^9\pm0.08\%$ electrons/s, derived from the global fit (case 4a in Table I). Uncertainties are smaller than the symbols.

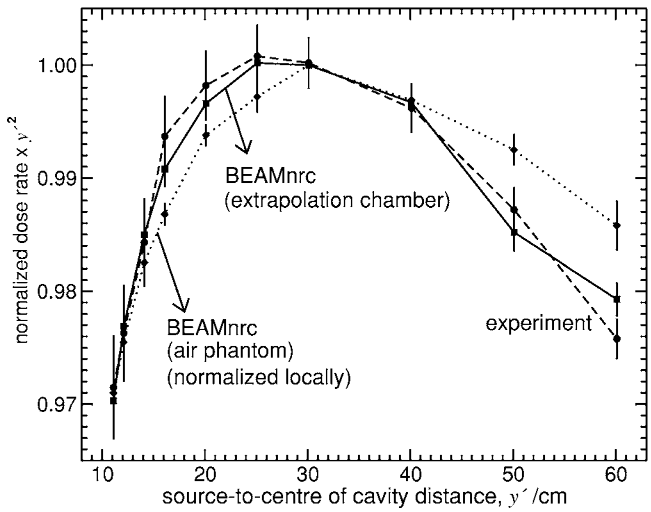

FIG. 8. Comparison of scaled Monte Carlo calculated and measured values of dose rate in a 0.2015 cm air cavity times y'^2 as a function of source-to-center of air-cavity distance, y'. The values are normalized by the scaled calculated value at $y=30$ cm times $(30.100\,75)^2$ The value used for scaling calculated values is $\alpha=2.4744\times10^9\pm0.08\%$ electrons/s, derived from the global fit (case 4a in Table I). A common systematic uncertainty of 0.1% arising from the depth offset uncertainty (2 μm) has not been included in the experimental values. Also shown is the calculated on-axis dose to air times y'^2 when the source irradiates a cylindrical air phantom of dimensions 100 cm × 100 cm (normalized at 30.100 75 cm).

2. Response vs chamber depth

Figure 9 presents the dose rate values normalized to D_{MC} for different chamber depths at $y=30$ cm. The effect on the measured dose rate of the 2 μm depth offset uncertainty is

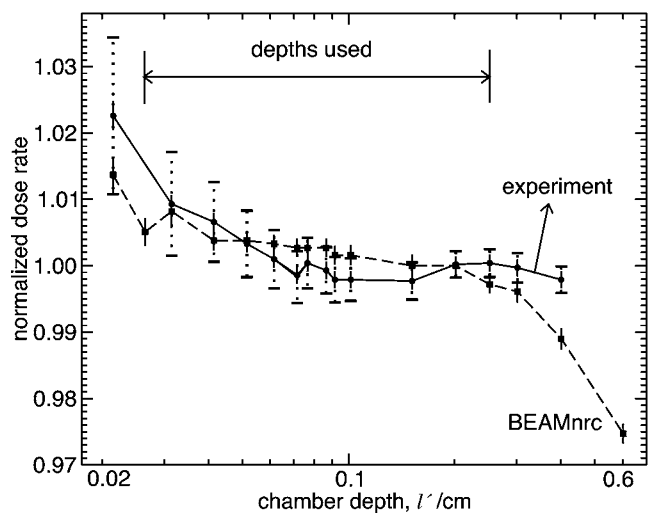

FIG. 9. Measured and scaled Monte Carlo calculated dose rates as a function of chamber depth at source-to-chamber distance, $y=30$ cm. Values are normalized to the scaled calculated dose rate at a depth of 0.2015 cm. The value used for scaling calculated values is $\alpha=2.4744\times10^9\pm0.08\%$ electrons/s, derived from the global fit (case 4a in Table I). The solid error bars on the measured response reflect all uncertainties except those from the uncertainty in the depth offset (2 μm), as well as a common systematic uncertainty of 0.13% arising from positioning of the chamber at $y=30$ cm. The effect of the depth offset uncertainty (2 μm) is shown by the dotted error bars with horizontal ends. ISO recommends using nominal depths between 0.025 and 0.25 cm (Ref. 4).

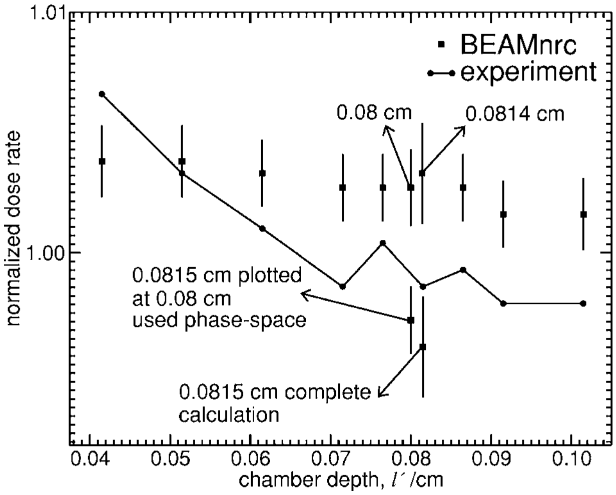

FIG. 10. Same as Fig. 9 for select chamber depth values to show the Monte Carlo artifact observed at a depth of 0.0815 cm. The 0.0815 cm artifact shows up in calculations based on the phase-space data (used for all other calculations shown) as well as in an independent complete simulation of the geometry. The 0.0815 cm point has also been repeated with a different random number sequence and gives the same result. The statistical uncertainty associated with the measured response is ±0.1% for all chamber depths shown. The measurements also suffer from a common systematic uncertainty of 0.13% arising from the positioning of the chamber at $y=30$ cm and the depth offset uncertainty of 2 μm for each chamber depth.

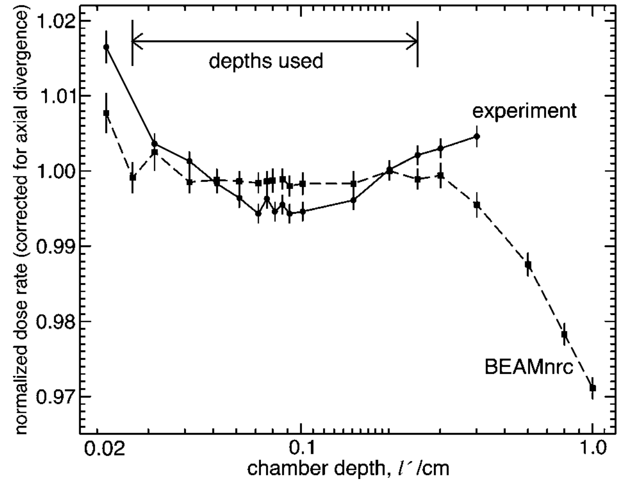

FIG. 11. Same as Fig. 9 but the dose rate values are corrected for axial divergence. The uncertainties on measured response do not include the effect of the 2 μm uncertainty in the depth offset or a common systematic uncertainty of 0.13% arising from the positioning of the chamber at $y=30$ cm.

represented by the dotted error bars and is large for the smaller depths. The uncertainties shown on the measured response do not include a 0.13% uncertainty arising from positioning error at $y=30$ cm. ISO recommends only using nominal depths between 0.025 and 0.25 cm,[4] and in this range the calculations agree with the measurements within 0.4%. At the smallest depth of 0.0215 cm there is reasonable agreement given the increased uncertainty due to the uncertainty in the depth offset. However, for larger depths there is a clear trend showing disagreement (discussed further below regarding Fig. 11). The same trend was observed for some preliminary data at $y=20$ cm.

Figure 10 is similar to Fig. 9 but with no uncertainty bounds on the measured data (for clarity) and for more depths in a smaller range. This shows an apparent artifact in the calculations at a depth of 0.0815 cm (plotted at 0.08 cm for the purpose of clarity), where the dose rate is less by 0.6% than the dose rate at 0.0814 cm. The calculation for the 0.0815 cm point has also been repeated with a different random number sequence and gives the same result. To ascertain whether this artifact is due to the use of phase-space files, a complete Monte Carlo simulation including the source was carried out. The result shows the same artifact. There is no artifact at 0.0815 cm when the extrapolation chamber is at $y=20$ cm.

In Fig. 9 the measured data appear to be more or less uniform for larger depths whereas the calculated data show a clear decreasing trend which superficially is unexpected. However, one of the first corrections required in the analysis of such data is a correction for beam divergence. To first order, for a relatively high-energy source such as $^{90}\mathrm{Sr}/^{90}\mathrm{Y}$, this correction requires multiplication of the dose by $(1+l'/y)$ and Fig. 11 shows the data so corrected. The experimental data are no longer flat but the calculated doses are flat over the range of depths recommended for use by ISO,[4] although not at depths greater than 0.3 cm. As a check that there is nothing wrong with our model, we ran a simulation with all chamber materials changed to air and the value of ECUT changed to 1 keV everywhere near the sensitive air-cavity region. Under these circumstances the dose to the air-cavity (corrected for divergence of the beam) was constant as the depth was varied. The lack of flatness in the calculated values outside the recommended depth range (Fig. 9) indicates that there are further, as yet unidentified, correction factors required. The lack of flatness in the experimental values, for depths larger than 0.25 cm may suggest that the electric field lines defining the chamber volume are becoming distorted.

3. Response vs added Mylar

Figure 12 presents the normalized dose rates as Mylar is added to the front of the extrapolation chamber. The uncertainties shown on the measured response do not include the systematic uncertainties of 0.1% arising from the 2 μm uncertainty in the depth offset at the depth of 0.2015 cm and 0.13% from positioning of the chamber at $y=30$ cm. The increase in dose value with added Mylar thickness is caused by multiple scattering of the electrons in Mylar. The maximum dose rate is observed at about 50 mg cm^{-2}. The calculated and measured responses agree within statistics of 0.46% for Mylar thicknesses up to 34.8 mg cm^{-2} (most values agree to within 0.2%). However, as the Mylar thickness increases from 52.1 to 146.1 mg cm^{-2}, the difference between the calculated and measured responses increases up to 1.2%. One possible explanation is that the air stopping powers used in the calculations are in relative error by 1.2% as the mean energy in the air cavity decreases from 778±0.2% keV to 688±0.3% keV to 633±0.3% keV for

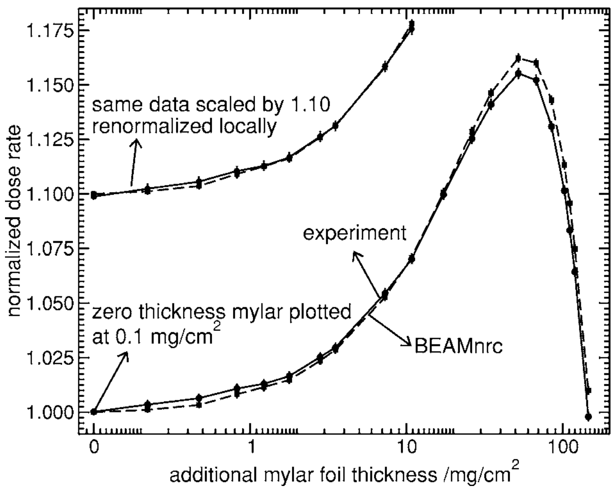

FIG. 12. Measured and scaled Monte Carlo calculated values of dose rate as a function of Mylar thickness added to the front of the extrapolation chamber for a source-to-chamber distance of $y=30$ cm and an air cavity of depth $l'=0.2015$ cm. Values are normalized to the scaled calculated value. The value used for scaling calculated values is $\alpha=2.4744 \times 10^9 \pm 0.08\%$ electrons/s, derived from the global fit (case 4a in Table I). The inset shown for select Mylar thicknesses utilized $\alpha=2.4774 \times 10^9 \pm 0.1\%$ electrons/s calculated based on the 10 dose values corresponding to 0–10.8 mg cm^{-2}. Normalization is done locally. The ordinates in the inset are scaled by 1.10 for presentation purposes. The uncertainties on the measured response do not include the common systematic uncertainty of 0.1% arising from depth offset uncertainty and 0.13% arising from the chamber positioning uncertainty.

added Mylar thicknesses of 0, 52.1, and 146.1 mg cm^{-2}. The restricted collisional stopping powers for air used in the cavity dose calculations change by 3.2% over this energy range. Another possibility is a problem with the Mylar stopping powers as the mean energy decreases. This does not affect other comparisons (dose versus distance and dose versus depth) as much where the change in the mean energy of the electrons in the cavity is not as significant. For example, the mean energy in the sensitive air cavity varies from $812 \pm 0.1\%$ keV to $746 \pm 0.2\%$ keV when y is increased from 11 to 60 cm. The restricted collisional stopping powers change by about 1% over this energy range.

Using the global scaling and normalization, the calculated and measured curves are systematically different for the thinnest regions of Mylar. However, it is the shape of the curve in this region which is most important. To address this issue of the shape of the curves, we used the value of α corresponding to the thinnest regions of Mylar, i.e., those less than 10.8 mg cm^{-2} (case 3a of Table I). Use of this value of α($=2.4774 \times 10^9 \pm 0.10\%$ electrons/s) instead of the global value for these thinnest regions of Mylar results in a 0.13% increase in the scaled calculated dose rate values. The inset shown in Fig. 12 is based on this approach (for the purpose of presentation the ordinate was further scaled by 1.10). The agreement improves to between 0.02% and 0.2% (most values within 0.04%) for the thinnest regions of Mylar.

To investigate the sensitivity of the calculations to the uncertainty in the thickness of the stainless-steel covering the source, we repeated the Monte Carlo simulations with a 0.0125-cm-thick stainless-steel cover for 6 Mylar thicknesses, viz., 0, 1.786, 52.1, 85.0, 111.3 and 146.1 mg cm^{-2}. The value of α calculated in this case is $2.7469 \times 10^9 \pm 0.35\%$ electrons/s [using Eq. (2)]. To compare the absolute scaled calculated dose rate values for the 0.0125 and 0.01 cm cases, the value of α was recalculated for the 0.01 cm case utilizing the same six Mylar thicknesses. The value of α thus obtained for the 0.01 cm case is $2.4622 \times 10^9 \pm 0.28\%$ electrons/s. This 12% difference in the value of α is consistent with a difference of 12% in the energy escaping through the front face of the source. The agreement between the scaled calculated dose rate values for the 0.0125 and 0.01 cm cases (for the investigated six Mylar thicknesses) ranges between 0.01% and 0.26%. This agreement implies that the calculated relative responses are insensitive to the uncertainty in the front stainless-steel thickness of the source. This is because an increase in the front stainless-steel thickness does not significantly alter the energy spectrum from the source (see Fig. 5), just its intensity.

VI. CONCLUSION

We have described a BEAMnrc Monte Carlo model capable of reproducing three different experimental situations involving measurements with the NRC extrapolation chamber in the field of a $^{90}Sr/^{90}Y$ beta source. We have described various techniques which improve the efficiency of the calculations by factors of 5.5 for dose versus source-to-chamber distance simulations and 6.7 when the phase-space files are used for fixed source-to-chamber distance (30 cm) simulations. In the case of dose versus source-to-chamber distance, the agreement between calculated and measured values is within 0.37% (most values within 0.1%). In the case of dose versus depth the agreement is good (within 0.4%) for the ISO-recommended range of nominal depths 0.025–0.25 cm. A systematic uncertainty of 2 μm in the depth offset leads to larger experimental dose rate uncertainties and therefore reasonable agreement with the calculations even for the smallest depth of 0.0215 cm. The agreement in terms of shape for the case where additional Mylar is added to the front face of the extrapolation chamber is very good up to 10 mg cm^{-2} (see inset in Fig. 12) although the agreement for thicker layers of Mylar is not perfect. However, it is the shape for thin Mylar layers that is most central to understanding correction factors. The agreement between calculated and measured responses is also not affected by the uncertainty in the front stainless-steel thickness of the source which only affects the absolute calculations. We conclude that the Monte Carlo model can be used for accurately estimating the various correction factors necessary to establish the dose to tissue from the measured dose to air. The measurements also provide a detailed benchmark of the use of the EGSnrc code system with beta sources.

ACKNOWLEDGMENTS

The research work is partially funded by Natural Sciences and Engineering Research Canada and the Canada Research Chairs Program. We thank our colleague Carl Ross for useful comments on the manuscript.

[a)]Electronic mail: drogers@physics.carleton.ca

[1]J. Böhm, "The perturbation correction factor of ionisation chambers in β-radiation fields," Phys. Med. Biol. **25**, 65–75 (1980).

[2]J. Böhm, "The National Primary Standard of the PTB for Realizing the Unit of the Absorbed Dose Rate to Tissue for Beta Radiation," Technical Report No. PTB-Dos–13, Physikalisch Technische Bundesanstalt, Braunschweig, Germany, 1986.

[3]L. Van der Zwan and K. W. Geiger, "The β-Calibration Facility at the National Research Council of Canada," NRC Report No. PIRS–0093, Ottawa, 1986.

[4]ISO, "Nuclear energy—Reference beta-particle radiations—Part 2: Calibrations fundamentals related to basic quantities characterizing the radiation field," International Standard ISO/FDIS 6980–2.2, ISO, Geneva, Switzerland (Draft, July 2004).

[5]IAEA, "Calibrations of photon and beta ray sources used in brachytherapy," Technical Report No. IAEA-TECDOC–1274, International Atomic Energy Agency, Vienna, Austria, 2002.

[6]B. Owen, "The beta calibration of radiation survey instruments at protection levels," Phys. Med. Biol. **17**, 175–180 (1972).

[7]I. Kawrakow and D. W. O. Rogers, "The EGSnrc Code System: Monte Carlo simulation of electron and photon transport," Technical Report No. PIRS–701, National Research Council of Canada, Ottawa, Canada, 2000.

[8]D. W. O. Rogers, B. A. Faddegon, G. X. Ding, C.-M. Ma, J. Wei, and T. R. Mackie, "BEAM: A Monte Carlo code to simulate radiotherapy treatment units," Med. Phys. **22**, 503–524 (1995).

[9]D. W. O. Rogers, C.-M. Ma, G. X. Ding, B. Walters, D. Sheikh-Bagheri, and G. G. Zhang, "BEAMnrc Users Manual," NRC Report No. PIRS 509(a)revF, 2001.

[10]G. X. Ding, D. W. O. Rogers, and T. R. Mackie, "Calculation of stopping-power ratios using realistic clinical electron beams," Med. Phys. **22**, 489–501 (1995).

[11]C.-M. Ma and S. B. Jiang, "Monte Carlo modelling of electron beams from medical accelerators," Phys. Med. Biol. **44**, R157–R189 (2000).

[12]D. Sheikh-Bagheri and D. W. O. Rogers, "Calculation of nine megavoltage photon beam spectra using the BEAM Monte Carlo code," Med. Phys. **29**, 391–402 (2002).

[13]F. Verhaegen and J. Seuntjens, "Monte Carlo modelling of external radiotherapy photon beams," Phys. Med. Biol. **48**, R107–R164 (2003).

[14]ICRU, "Dosimetry of External Beta Rays for Radiation Protection," ICRU Report No. 56, ICRU, Washington, DC, 1997.

[15]D. W. O. Rogers, I. Kawrakow, J. P. Seuntjens, and B. R. B. Walters, "NRC User Codes for EGSnrc," Technical Report No. PIRS-702, National Research Council of Canada, Ottawa, Canada, 2000 (see http://www.irs.inms.nrc.ca/inms/irs/EGSnrc/EGSnrc.html).